SAND2018-0432

SANDIA REPORT
SAND2014-2017
Unlimited Release
Printed October 2017

Electrochemical Detection of Single Molecules in Nanogap Electrode Fluidic Devices

Jeri Timlin, Stephen Anthony, Susan Rempe, Mangesh Chaudhari, Phil Miller, Matthew Moorman, John Anderson, Gaddi Haase, and Ronen Polsky

Prepared by
Sandia National Laboratories
Albuquerque, New Mexico 87185 and Livermore, California 94550

Sandia National Laboratories is a multimission laboratory managed and operated by National Technology and Engineering Solutions of Sandia, LLC, a wholly owned subsidiary of Honeywell International, Inc., for the U.S. Department of Energy's National Nuclear Security Administration under contract DE-NA0003525.

Sandia National Laboratories

Issued by Sandia National Laboratories, operated for the United States Department of Energy by National Technology and Engineering Solutions of Sandia, LLC.

Available to DOE and DOE contractors from
U.S. Department of Energy
Office of Scientific and Technical Information
P.O. Box 62
Oak Ridge, TN 37831

Telephone: (865) 576-8401
Facsimile: (865) 576-5728
E-Mail: reports@osti.gov
Online ordering: http://www.osti.gov/scitech

Available to the public from
U.S. Department of Commerce
National Technical Information Service
5301 Shawnee Rd
Alexandria, VA 22312

Telephone: (800) 553-6847
Facsimile: (703) 605-6900
E-Mail: orders@ntis.gov
Online order: https://classic.ntis.gov/help/order-methods/

SANDIA REPORT
SAND2014-2017
Unlimited Release
Printed October 2017

Electrochemical Detection of Single Molecules in Nanogap Electrode Fluidic Devices

Jeri Timlin, Stephen Anthony, Susan Rempe, Mangesh Chaudhari, Phil Miller, Matthew Moorman, John Anderson, Gaddi Haase, and Ronen Polsky

Sandia National Laboratories
Nano and Micro Sensors Department
P. O. Box 5800
Albuquerque, New Mexico 87185-MS0892

Sandia National Laboratories
Nano and Micro Sensors Department
P. O. Box 5800
Albuquerque, New Mexico 87185-MS0892

Abstract

The purpose of this project was to gain a fundamental understanding of molecular diffusion in nanogap electrodes and the diffusive behavior of single molecules undergoing electron transfer. Electrochemical methods for single molecule detection have remained elusive due to the vanishingly small currents involved in single molecule electron transfer. Electrochemical detection of single molecules undergoing redox cycling would enable detection of single enzymes, proteins, and DNA strands resulting in new and improved ultrasensitive sensing devices impacting Detection At The Limits research challenge (DATL), supporting needs in DHS and DoD. We attempted to integrate orthogonal validation techniques, Total Internal Reflection Fluorescence Microscopy (TIRF), and molecular simulation to clarify (1) the mechanism leading to current build up due to redox cycling and (2) diffusion and adsorption of single molecules undergoing redox reactions. While creation of nanogap electrodes with transparent windows was ultimately successful in this project (along with TIRF demonstration of single molecule imaging), time and methods constraints did not allow final electrochemical measurements to be coupled for simultaneous interrogation.

TABLE OF CONTENTS

1. Imaging Effectiveness Calculator for Non-Design Microscope Samples

Abstract

When attempting to integrate single molecule fluorescence microscopy with microfabricated devices such as microfluidic channels, fabrication constraints may prevent using traditional coverslips. Instead, the fabricated devices may require imaging through material with a different thickness or index of refraction. Altering either can easily reduce the quality of the image formation (measured by the Strehl ratio) by a factor of two or more, reducing the signal-to-noise ratio accordingly. In such cases, successful detection of single molecule fluorescence may prove difficult or impossible. Rather than experimentally determining feasibility, the effect of imaging through non-design materials can be theoretically calculated using the Gibson and Lanni point spread function (PSF). However, the relationship between non-design inputs to the Gibson and Lanni PSF and the resulting Strehl ratio is not intuitive since the Gibson and Lanni PSF requires calculating the integral of a complex-valued function. Here we provide software to calculate the effect of non-design materials upon the Strehl ratio or ensquared energy and explore the impact of common materials used in microfabrication.

Introduction

Individually, both single molecule microscopy[1] and microfluidics[2] have commanded substantial interest in recent years. The combination of the two, single-molecule fluorescence detection in microfluidic channels, has been suggested to be “the Holy Grail” of micro total analysis systems (μTAS).[3] While single molecule fluorescence detection in microfluidic channels has been demonstrated on a number of occasions[4, 5], several factors render these experiments particularly challenging. To begin with, the signal-to-noise ratio (SNR) is frequently extremely low when imaging single fluorophores, such that an SNR of >5 is considered a high SNR and a SNR of 2 is not uncommon.[6] As such, single molecule fluorescence microscopy inherently operates near the limits of detectability. Second, the integration of microfluidics with imaging is itself challenging.[5] However, one factor that is often overlooked in this field is the impact of non-design coverslips on the microscope image formation.

The high numerical aperture (NA) objectives commonly used for single molecule fluorescence imaging are precision optics, most of which are designed to be used with borosilicate coverslips 170 µm thick (#1.5 coverslips). Deviations from the specified coverslip generally introduce optical aberrations, particularly spherical aberration, which decrease the image quality. Unfortunately, borosilicate glass does not readily lend itself to microfabrication. On the other hand, while silicon is one of the preferred materials for microfabrication, it is opaque to visible light. As a result, when imaging through a microfabricated material is required, some of the most commonly selected materials are quartz, fused silica, Borofloat 33 (Pyrex), or polydimethylsiloxane (PDMS). Unfortunately, the index of refraction of these compounds (~1.4 to 1.47 at 532 nm) differs substantially from that of a design coverslip (1.526 at 532 nm).

At first glance the difference in index of refraction compared to design coverslips may appear to be a minor difference; after all, when looking through a rectangular sheet of these materials by eye, they are practically indistinguishable. However, most microscopists are well aware that image quality degrades substantially when imaging several microns into an aqueous sample using an oil immersion objective. While the index of refraction difference between the index of refraction of immersion oil ($n_{oil} \approx 1.518$) and water ($n_{water} \approx 1.33$) is roughly three times larger than the difference between the design and non-design coverslips, the difference in index of refraction is for a layer over 100 µm thick instead of just a few microns. As such, the change in the quality of the focus due to a non-design coverslip should be expected to be even more significant.

Complicating the matter, using a non-design coverslip may alter the ideal focal position. By altering the focal position of the microscope (the thickness of the immersion oil layer) it may be possible to partially cancel the aberrations the aberrations introduced by the non-design coverslip.[7] While the aberrations are unlikely to perfectly cancel, "Rayleigh's quarter wavelength rule states that if the maximum value of an aberration function is less than a quarter of an illumination wavelength the intensity at the focus is changed by a small amount which is considered to be tolerable."[8] As such, even though the altering the thickness of the immersion oil may only partially cancel the aberrations, in some circumstances that may be sufficient to restore sharp focus.

Fortunately, an analytical model exists for the aberrations introduced by differences between the actual acquisition conditions and the design conditions of microscope objectives.[9] While the initial model by Gibson and Lanni was based upon scalar diffraction theory, it has since been extended to vector diffraction theory.[7] For our purposes, though, scalar diffraction theory is sufficient and is used for all calculations in this work. In short, using existing optical theory it is possible to compute the entire point spread function (PSF) for non-design coverslips of arbitrary thickness and focal depth.

Two convenient measures of the focal quality, the Strehl ratio and the ensquared energy, can be readily calculated from the PSF. While related, each of these measures offers advantages. The Strehl ratio can be defined as the ratio of the peak intensity of the aberrated point source relative to the peak intensity of the corresponding diffraction limited system for the same aperture.[10] As such, the Strehl ratio for any system conveniently ranges between 0 and 1, where the Strehl ratio equals 1 only for ideal optical systems. One common criterion for a well-functioning optical system is Marechal's criterion, which requires the Strehl ratio to be greater than 0.8.[8]

An alternate measure of the focal quality is the ensquared energy, defined as the fraction of the total PSF intensity which is within a centered square of a specified size (centered on the centroid of the PSF). Possible values for the ensquared energy also range from 0 to 1, but in this case the ensquared energy for any PSF will be 1 if the square is sufficiently big. As such, in order to compare the quality of image formation for different PSFs, it is necessary to specify a fixed size for the square. For digital microscopy, a convenient size square to employ is the detector pixel size; throughout the rest of this work, the ensquared energy will refer to the ensquared energy for a pixel. In some ways, the ensquared energy per pixel is a more practical measure than the Strehl ratio. By accounting for the pixel size, this measure quantifies the impact on the peak signal that would be experimentally observed. For example, if the detector has particularly large pixels, it is possible that the PSF would be almost entirely contained within a single pixel (ensquared energy ≈ 1) even when the Strehl ratio reduces from 1.0 to 0.75. At the same time, the Strehl ratio is often easier to interpret; the ideal Strehl ratio is always 1.0, but the ensquared energy per pixel may be much less than 1, even for perfect optics.

While the Strehl ratio and the ensquared energy provide convenient measures of the imaging quality, how non-design parameters in the Gibson and Lanni PSF effect these measures is not intuitive. Determining the Gibson and Lanni PSF requires calculating the integral of a complex valued function containing a Bessel function. Therefore, determining the Strehl ratio and ensquared energy is not straightforward and may fall outside the normal areas of expertise of scientists simply interested in knowing how using a non-design coverslip will affect their image quality. While a convenient PSF calculator exists which supports multiple PSF models including the Gibson and Lanni model,[11] their implementation is intended for the common case of focusing on fluorophores away from the coverslip. As such, while their software allows the depth inside the sample to be varied, it does not allow for non-design coverslips. A more recent work allows all the Gibson-Lanni parameters to be varied and the PSF to be rapidly calculated,[12] but is not optimized for multiple calculations with different coverslip conditions. In this work, we explore the effect of common microfabrication materials on the image quality, including whether image quality can be restored by independently altering the thickness of the non-design coverslip and the focal depth. Additionally, we develop and provide software to calculate the Gibson and Lanni PSF, Strehl ratio, and ensquared energy, allowing non-design immersion, coverslip, and sample layers. While primarily directed at microfabricated channels where it is more difficult to use commercially available coverslips, this calculator is relevant whenever non-design coverslips or other media are used.

Gibson and Lanni Model

The Gibson and Lanni PSF model is a generalization of the Born and Wolf PSF model allowing for refractive index mismatches between the design and experimental optical system. A detailed analysis of the relationship between the Gibson-Lanni and Born-Wolf models is available in Appendix A of [11]. In brief, the Gibson-Lanni model includes a phase term accounting for spherical aberrations up to second order. The spherical aberrations may be induced by differences between the design and experimental optical system in the refractive indices, the layer thicknesses, or a combination of the two. The typical formulation assumes three optical layers, corresponding to the microscope sample or specimen, the coverslip, and the immersion media (See Figure 1). The standard Gibson and Lanni model uses scalar diffraction theory and assumes that the index of refraction is constant within a layer. These assumptions and approximations are sufficient for our purposes and are used throughout this work. However, the Gibson and Lanni model has been extended to vector diffraction theory,[7] arbitrary numbers of layers,[13] and variable refractive indices within layers.[13]

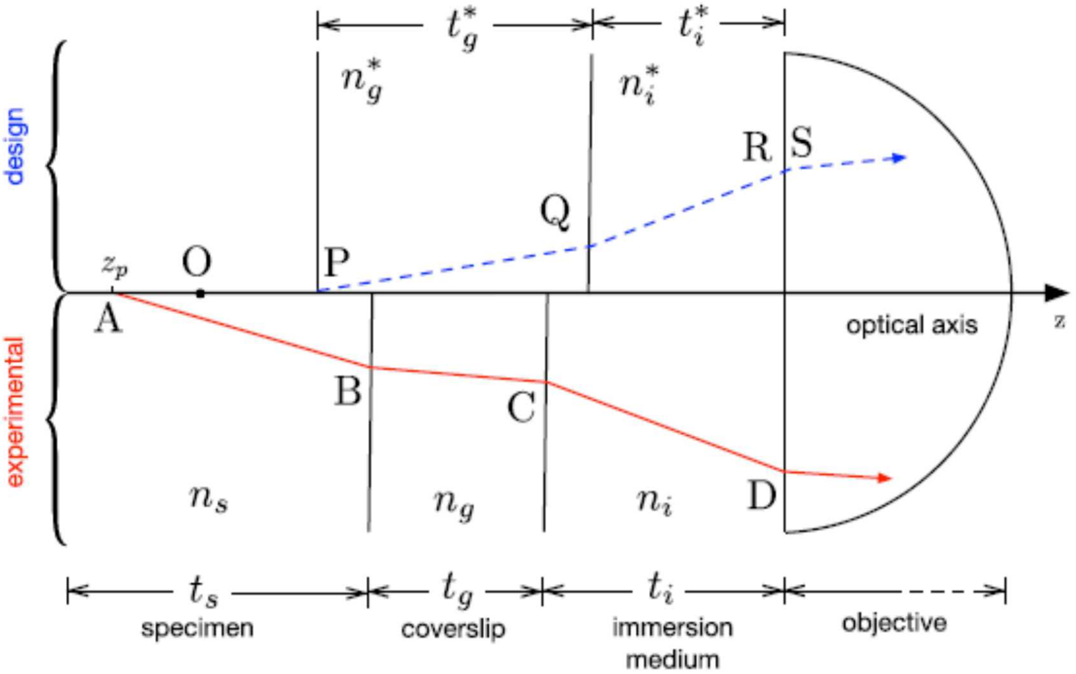

Figure 1

The Gibson-Lanni model accounts for three optical layers: the sample layer, the coverslip layer, and the immersion layer. For each layer, the design and actual refractive index and thickness must be specified. The design conditions for the sample layer are not shown, as the design thickness of the sample layer is 0. Design (dashed line) and actual (solid line) rays entering the front of the microscope objective travel different optical paths. The optical path difference between the design and actual ray can be computed as OPD = [ABCD] – [

Throughout this work, we will only consider the PSF of the intensity, as this is what is typically measured in the microscope. Since the Gibson-Lanni PSF is shift invariant in the lateral direction, we will express it in terms of *r*(θ), where *r*(θ) corresponds to the apparent lateral position relative to the point source in the image plane. The Gibson-Lanni PSF is given by:

$$I(\theta) = \left| C \int_0^1 J_0[kNA\rho r] \times e^{iW(\rho)} \times \rho \, d\rho \right|^2$$

$$r = \sqrt{x^2 + y^2}$$

$$W(\rho) = k\left[n_s t_s\sqrt{1-\left(\frac{NA\rho}{n_s}\right)^2} + n_g t_g\sqrt{1-\left(\frac{NA\rho}{n_g}\right)^2} + n_i t_i\sqrt{1-\left(\frac{NA\rho}{n_i}\right)^2} - n_g^* t_g^*\sqrt{1-\left(\frac{NA\rho}{n_g^*}\right)^2} + n_i^* t_i^*\sqrt{1-\left(\frac{NA\rho}{n_i^*}\right)^2}\right]$$

where the terms in Equation 1 are defined in Table 1.

Parameter	Description
I(theta)	Intensity of the PSF for the specified parameters
C	A normalizing constant
J0()	Zeroth order Bessel function of the first kind
k	2 pi/lambda
lambda	Wavelength of the emitted light (in vacuum)
NA	Numerical aperture of the microscope
x,y	The apparent lateral positions relative to the point source in the image plane
r	The apparent radial position relative to the point source in the image plane
i	sqrt(-1)
ns	Refractive index of the actual sample (or specimen) layer
ns*	Refractive index of the design sample layer.
ts	Thickness of the actual sample layer imaged through (axial position of the point source within the sample l
ts*	Thickness of the design sample layer imaged through
ng	Refractive index of the actual coverslip
ng*	Refractive index of the design coverslip
tg	Thickness of the actual coverslip
tg*	Thickness of the design coverslip
ni	Refractive index of the actual immersion media layer
ni*	Refractive index of the design immersion media layer
ti	Thickness of the actual immersion media layer
ti*	Thickness of the design immersion media layer
W	The Gibson and Lanni phase aberration

Table 1

Parameter descriptions

Microscope objectives are designed to either image at the interface between the sample and the coverslip or to image into a sample whose index of refraction equals that of the immersion medium. An example of the latter case is using a water immersion objective to image into an aqueous sample in order to be able to focus effectively deeper into the sample. From the perspective of the Gibson-Lanni model, though, the two cases are equivalent although in reality there would, of course, be slight differences not captured by the model including Fresnel reflections at the extra interfaces. The Fresnel reflections also result in slight differences between the excitation and detection PSFs.[14] Examining the model shows that all layers with the same index of refraction can effectively be combined, acting equivalently to a single layer with the same total thickness and index of refraction. Similarly, the order of the layers does not matter for the Gibson-Lanni model. As a consequence, there is no need to include terms for the design sample layer thickness in W; either its thickness is zero or it has the same index of refraction as the immersion layer and can be combined with that layer.

One scenario that bears special mentioning is total internal reflection, which can limit the effective numerical aperture or place constraints on the allowable indices of refraction for various layers. Total internal reflection occurs when light propagates from an optically denser medium into a less dense one at an angle greater than the critical angle. The critical angle is defined as $\theta_{critical} = \sin^{-1}\left(\frac{n_1}{n_2}\right)$ where $n_2 > n_1$, where total internal reflection fluorescence (TIRF) microscopy requires that the angle of incidence of the excitation beam be above the critical angle. For objective-based TIRF microscopy, this requires high numerical aperture objectives, where the numerical aperture is defined as "the sine of the angular semiaperture in the object space multiplied by the refractive index of the object space, $NA = n\sin(\theta)$."[10] Immediately, it can be seen that when imaging into an aqueous sample, the maximum possible numerical aperture is equal to the index of refraction of water, $n_{water} \approx 1.33$. However, high NA objectives commonly used for imaging aqueous samples in biology frequently list numerical apertures greater than that, often 1.4 to 1.46. This apparent discrepancy occurs for two reasons. First, if the goal when designing the objectives is to collect the maximum amount of light, the numerical aperture of the objective should be at least equal to the refractive index of the object space. While exceeding the refractive index of the object space does not result in greater light collection, anything less reduces the amount of light captured. Meanwhile, the exact target value varies between samples; while the refractive index of pure water is approximately 1.33, the refractive index of normal cells is typically 1.35-1.37 while the refractive index of cancerous cells often approaches 1.4.[15] So, while the higher objective NA may not improve the image quality for some samples, it is necessary to obtain optimum images from all samples. Second, objective-based total internal reflection

(TIRF) microscopy is only possible if the nominal objective NA is higher than the index of refraction of the sample layer, allowing total internal reflection to occur. Given the range of indices of refraction in biological samples, reliably obtaining TIRF conditions may be difficult unless the objective has an NA greater than 1.4. However, from the perspective of light collection and the resulting PSF, the effective NA is clearly limited to the lesser of the objective NA or the lowest index of refraction material it passes through. Additionally, for objective-based TIRF microscopy to occur, the index of refraction of the sample layer must be below that of any other layers and below the nominal NA of the objective. For convenience, when the software provided with this work is given the objective NA as an input, the effective NA for the PSF is calculated by the software. A mathematically equivalent way of limiting the effective NA is used by Li et al.[12] They reduce the integration range of ρ, such that the integration range is not always $\rho \in [0,1]$.

Microfabrication Indices of Refraction

For convenience, the indices of refraction of a number of materials commonly employed in biological microscopy or microfabrication are collected here. Of course, the refractive index of materials varies with the wavelength of the light, a phenomenon known as dispersion. For purposes of this work we have standardized on using the indices of refraction at 532 nm, a common laser line. In some cases, it was possible to directly obtain the index of refraction at 532 nm, n_{532}, from the reference. Other times, it was only possible to obtain the index of refraction and reciprocal dispersion (Abbe number) at a different wavelength. The formula for the Abbe number V_d is

$$V_d = \frac{n_d - 1}{n_F - n_C}$$

where n_d, n_F, and n_C are the refractive indices at the helium d-line ($\lambda_d \approx$ 587.56 nm), the hydrogen F-line ($\lambda_F \approx$ 486.13 nm) and the hydrogen C-line ($\lambda_C \approx$ 656.27 nm) respectively.[16] When the index of refraction and the reciprocal dispersion are known for a particular wavelength, the chromatic dispersion $\frac{\partial n}{\partial \lambda}$ can be calculated using the assumption that the dispersion is linear between the reference wavelengths in the denominator. For example, given V_d and n_d for a compound, the chromatic dispersion for that compound would be approximated as

$$\frac{\partial n_d}{\partial \lambda} \cong \frac{n_F - n_C}{\lambda_F - \lambda_C} = \frac{n_d - 1}{V_d(\lambda_F - \lambda_C)}$$

Using the chromatic dispersion, the approximate index of refraction at any other wavelength can be calculated, where the index of refraction at 532 nm, n_{532} would be calculated as

$$n_{532} \cong n_d + \frac{\partial n_d}{\partial \lambda}(532\ \mathrm{nm} - \lambda_d)$$

Of course, the accuracy of these approximations will depend upon how linear the dispersion is and will tend to be more accurate the closer the reference wavelength (e.g. n_d) is to the desired wavelength (e.g. n_{532}). Frequently, the refractive index and Abbe number are specified for a different wavelength such as the mercury e-line ($\lambda_e \approx 546.07$ nm) which is often easier to measure. The reference wavelengths and corresponding formula for the Abbe number V_e are defined in ISO standard 7944.[17]

Table 2 provides the indices of refraction for various compositions of borosilicate glass, the material typically used for microscope coverslips. The range of refractive indices in this table, from 1.5190 to 1.6109 at 532 nm, shows that for precision optical systems specifying the general type of glass is insufficient. Instead, the exact material employed or the refractive index must be specified. Of the borosilicate glasses listed in Table 2, only Schott D263M and the material used in Zeiss high performance coverslips meet the ISO 8255-1 specifications for microscope coverslips.[18] Table 3 provides the indices of refraction for a number of materials commonly used in microfabrication or microscopy.

Imaging Quality

Figure 2 shows the effect of non-design coverslip thickness and index of refraction on the Strehl ratio and ensquared energy at the best focus. All calculations were performed for a 60X oil immersion TIRF objective (Olympus Plan APO, NA 1.45) with a working distance of 100 μm and designed for use with #1.5 coverslips. Calculations were performed for TIRF excitation into an aqueous solution ($n_s = 1.3337$), calculating the PSF and imaging quality for fluorophores emitting at 532 nm. The pixel size of the simulated detector (Andor Technologies, Inc, iXon 887) was 16 μm. For each coverslip thickness of the various

Material	n532	ne	ve
Ohara- BSM (borosilicate, medium index)	1.6109		
Zeiss High Performance Coverslips	1.5263	1.5255	56
Schott D263M (borosilicate)	1.5263	1.5255	55
Hoya - BSD (borosilicate crown)	1.5195		
Hikari - BK (borosilicate crown)	1.5195		
Schott - BK (borosilicate crown)	1.5195		
Ohara - BSL (borosilicate, low-index)	1.5190		
Sumita - BK (borosilicate crown)	1.5190		

Table 2: Borosilicate indices

compounds, the best focus was determined by calculating the immersion oil thickness for standard immersion oil ($n_i = n_i^* = 1.519$) which produced the highest Strehl ratio. For materials where $n_g \leq n_i^*$, the Strehl ratio and ensquared energy abruptly decrease when the coverslip thickness exceeds ~250 µm, where the exact transition depends upon the material. Detailed examination shows that unsurprisingly, as the coverslip thickness increases, the optimum immersion oil thickness (best focus) occurs at an ever decreasing immersion oil thickness. At some point, the optimum immersion oil thickness reaches zero. At that point, it is no longer possible to decrease the immersion oil thickness to compensate for increasing the coverslip thickness. As such, the amount of spherical aberration increases rapidly from that point, resulting in an abrupt drop in the Strehl ratio.

When varying the index of refraction of the coverslip, two clearly distinct ranges are observed: when $n_g \leq n_i^*$, and when $n_i^* < n_g$ (see Figure 3a). In the former case, obtaining a high Strehl ratio (above 0.8, Marechal's criterion) is theoretically impossible, and the optimum coverslip thickness is zero (see Figure 3b). In this region, the refractive index of both the immersion oil (n_i^*) and actual coverslip (n_g) differ from that of the design coverslip (n_g^*), so replacing any portion of the design coverslip with either of these materials will induce spherical aberration. However, since both n_i^* and n_g are less than n_g^*, both will produce the same sign of spherical aberration. As such, replacing part of the design coverslip layer with each material offers no benefit as no portion of the spherical aberration from these materials would cancel. As such, optimum imaging when $n_g < n_i^*$ is obtained by replacing the entirety of the design coverslip layer with immersion oil as the mismatch between n_i^* and n_g^* is less than the

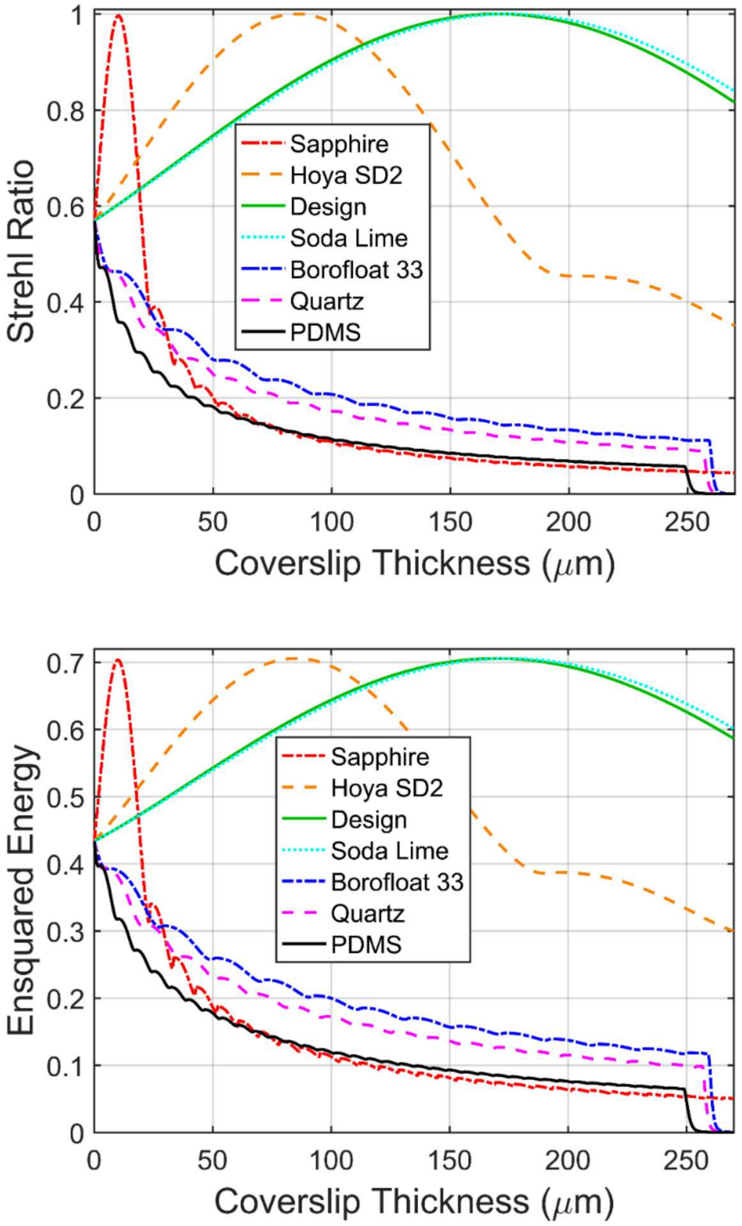

Figure 2

The Strehl ratio (a) and ensquared energy (b) calculated for a variety of potential coverslip materials at the best focus (optimum immersion oil thickness).

mismatch between n_g and n_g^*. The boundary where $n_g = n_i^*$ represents a special case; here, the index of refraction of the actual coverslip exactly matches the index of refraction of the immersion oil, so the two are perfectly interchangeable.

In the alternate case when $n_i^* < n_g$, maintaining a high Strehl ratio is theoretically possible (at least until the refractive index of the coverslip reaches implausibly high values). This case can be further divided into two subcases: when $n_i^* < n_g < n_g^*$, and when $n_g^* < n_g$. When $n_g^* < n_g$, reducing the actual coverslip thickness compared to the design coverslip thickness results in two regions of non-design index of refraction. In one of the regions, some of the design coverslip has been replaced with non-design coverslip, increasing the index of refraction. In the other region, some of the design coverslip has been replaced with immersion oil, increasing the index of refraction. While both of these regions will produce spherical aberration, since their sign is different the spherical aberrations will partially cancel each other. A similar phenomenon occurs when employing a non-design coverslip whose index of refraction is between that of the design coverslip and the immersion oil. In this subcase, increasing the coverslip thickness results in two regions of non-design index of refraction, where once again the sign of the mismatch differs between the two regions. Therefore, in either situation it is theoretically possible to maintain a high Strehl ratio for a non-design coverslip by adjusting the coverslip thickness. This analysis also suggests some potential option for improving the Strehl ratio when imaging either when $n_g \leq n_i^*$ or far into a sample where $n_s < n_i^*$. In either case, offsetting spherical aberrations are impossible to produce without introducing additional non-design elements. In either case, using a non-design immersion oil where $n_i^* < n_i$ would introduce spherical aberrations of the opposite sign, which could potentially partially cancel and reduce the overall aberration. When $n_s < n_i^*$, another possible option would be to use a thicker coverslip than specified by the microscope objective, effectively replacing some of the immersion layer with coverslip.

While theoretically possible to maintain a high Strehl ratio when $n_i^* < n_g$, in practice that may not always prove possible. Examining Figure 3b reveals that depending upon the actual coverslip index of refraction, obtaining the optimum Strehl ratio may require an implausibly thin coverslip or immersion oil layer. In order for a sapphire coverslip to satisfy Marechal's criterion, the coverslip would need to be less than 20 μm thick (see Figure 2a). Employing such a thin coverslip would not generally be feasible, as a coverslip that thin would be incredibly fragile, difficult to fabricate and prone to breakage if used. On the other hand, when n_g is only slightly greater than n_i^*, the optimum immersion oil thickness approaches 0. As the desired immersion oil thickness decreases, the risk of crashing the microscope objective into the coverslip increases dramatically. Additionally, beyond a certain point the viscosity of the immersion oil will make it difficult to decrease the immersion oil thickness without waiting a long time for it to equilibrate. As such, it can also be useful to consider what Strehl ratio can be obtained for a coverslip of design thickness (170 µm) as the index of refraction is varied (see Figure 4). While Figure 4 illustrates the effect of a mismatch in index of refraction of the coverslip while otherwise obeying the design constraints, a similar effect would be observed for a mismatch in index of refraction of the immersion oil. Since the refractive index of immersion oil is temperature dependent, imaging at 37°C using standard immersion oil (designed for 23°C) would have a similar effect, explaining why special immersion oil designed for imaging at 37°C is available.

Note that the amount of spherical aberration depends strongly on the numerical aperture; since the range of angles of incident light is much higher for high NA objectives, aberrations are much more pronounced. Figure 5 shows that for an objective with an NA of 0.8, imaging quality (as measured by either the Strehl ratio or ensquared energy) does not vary much between design and non-design coverslips. Figure 5 also highlights an important difference between the Strehl ratio and ensquared energy. While the maximum Strehl ratio is the same for the design coverslip regardless of NA, the maximum ensquared energy decreases from ~0.7 to ~0.4. This difference reflects the fact that the Strehl ratio measures peak intensity relative to a diffraction limited spot for the same NA, effectively compensating for changes in NA. In general, the Strehl ratio is more convenient for evaluating performance for a given microscope objective under different conditions. However, Figure 4 shows that even for a single microscope objective, the Strehl ratio and ensquared energy are not perfectly correlated. When trying to determine the effect changing an imaging parameter will have on the observed signal-to-noise ratio, the ensquared energy is a more reliable measure.

The extensive availability and common use of quartz coverslips could erroneously lead researchers to assume that quartz coverslips are generally fine for imaging. From a microfabrication standpoint, quartz is much more commonly employed than borosilicate or soda lime glass, which would also tend to favor its selection. However, Figure 2b shows that

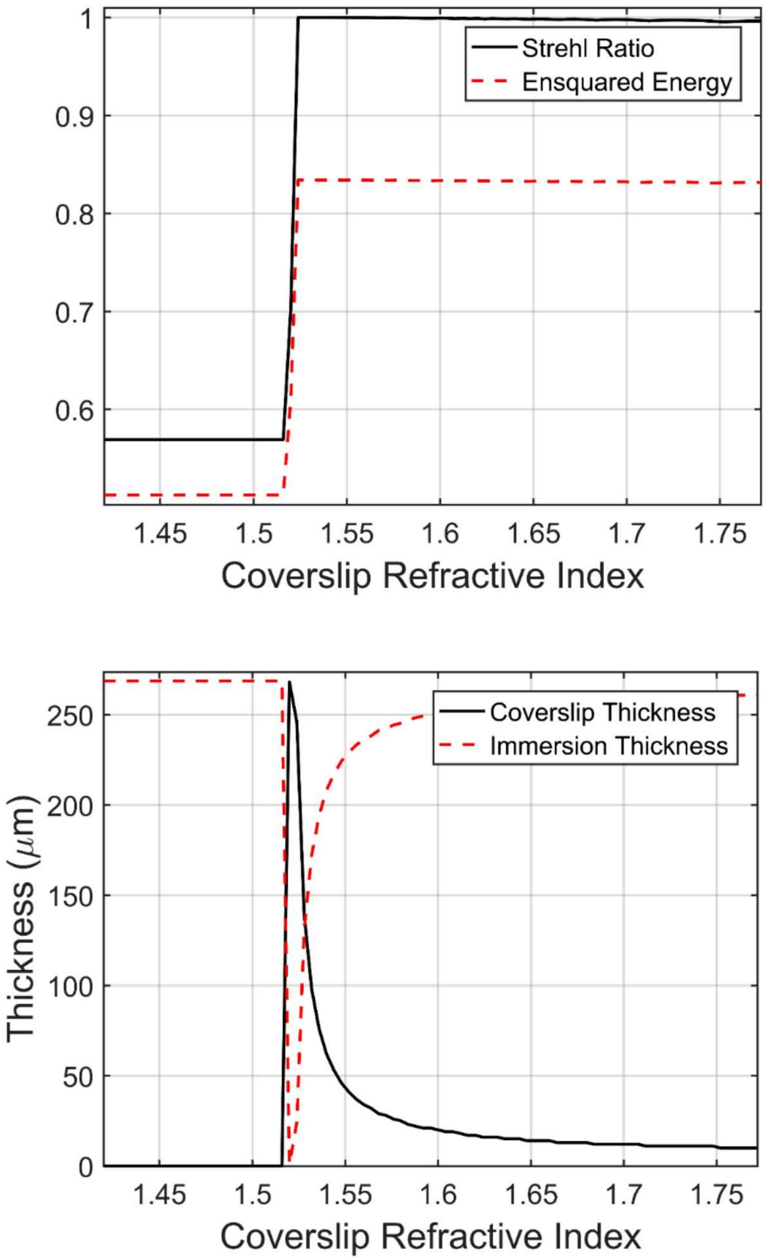

Figure 3

a) The best obtainable Strehl ratio and ensquared energy depending upon the refractive index of the coverslip.

b) The coverslip and immersion oil thickness required to maximize the Strehl ratio depending upon the refractive index of the coverslip.

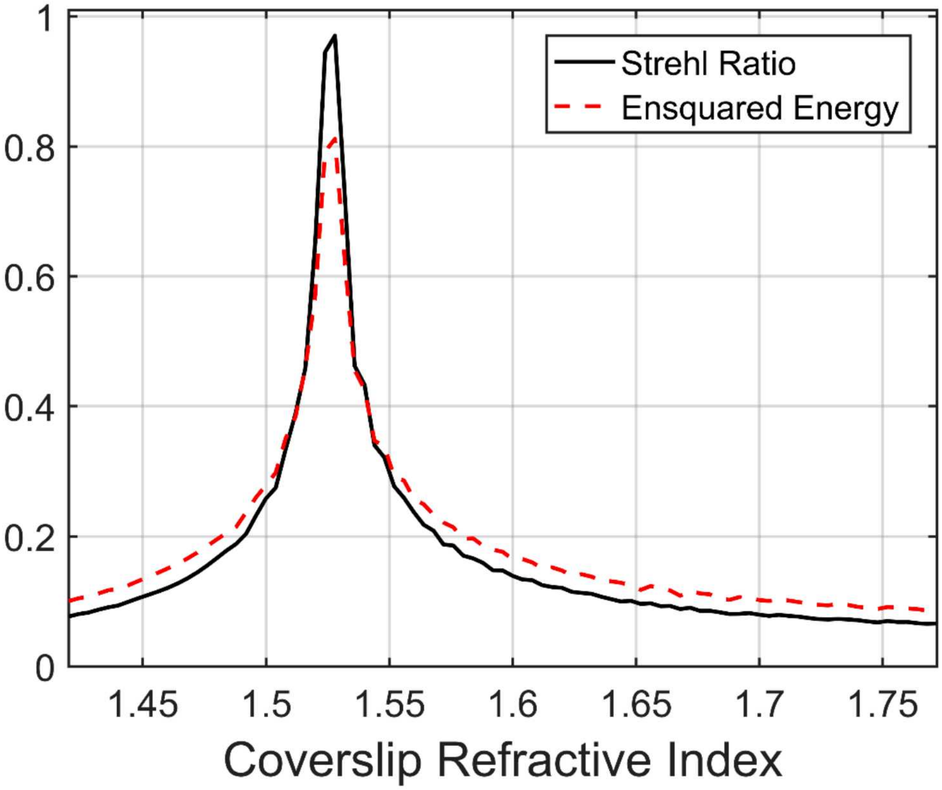

Figure 4

The best obtainable Strehl ratio and ensquared energy for a 170 micron coverslip depending upon the refractive index of the coverslip.

using a quartz coverslip with an NA 1.45 objective will result in a roughly fivefold reduction in the ensquared energy (and signal-to-noise ratio). Why would anyone use quartz coverslips if it can degrade imaging performance so substantially? To begin with, the UV absorption of standard microscope coverslips makes quartz coverslips a necessity when using UV. Additionally, in many circumstances the reduction in signal can either be tolerated, compensated for, or is otherwise less significant. In particular, Figure 5b indicates that for an NA 0.8 objective, when using a quartz coverslip, the ensquared energy is >90% of the ensquared energy for the design coverslip. In fact, the ensquared energy for a 170 μm quartz coverslip is actually higher for an NA 0.8 objective than for an NA 1.45 objective. Since the definition of high NA is fuzzy, depending upon the NA quartz coverslips can therefore be considered suitable for high NA imaging. Similarly, while signal-to-noise ratio is a major concern when performing single molecule fluorescence imaging, limited signal is rarely a problem when performing bright field imaging. Finally, the signal-to-noise ratio can potentially be increased by either increasing the acquisition time or the lased excitation power. As such, it is possible to perform single-molecule fluorescence microscopy with an NA 1.45 objective; it may simply require using ~10 times higher laser intensity than typically employed.[4] However, while increasing the detector integration time or laser power may sometimes be possible, the associated drawbacks may make this infeasible. While increasing the laser power can increase the number of photons per second emitted by the fluorophore, doing so will also increase how quickly the fluorophore will photobleach. Increasing the integration time will increase the signal-to-noise at the expense of the temporal resolution. Additionally, single molecule fluorescence microscopy often requires careful attention to the photon budget; only a limited number of photons can be obtained from a fluorophore before it irreversibly bleaches. In contrast, improving the ensquared energy improves the signal-to-noise ratio without consuming any additional photons from the limited photon budget.

The conclusions of this study were experimentally validated by comparing the PSFs observed for quartz, soda lime, and ISO 8255 borosilicate coverslips. The prior calculations were designed to match our actual experimental conditions (Olympus Plan APO 60X NA 1.45 with a

100 μm working distance, Andor Technologies, Inc, iXon 887 with a 16 μm pixel size). Excitation was performed using a 532 nm laser (fill in more details).

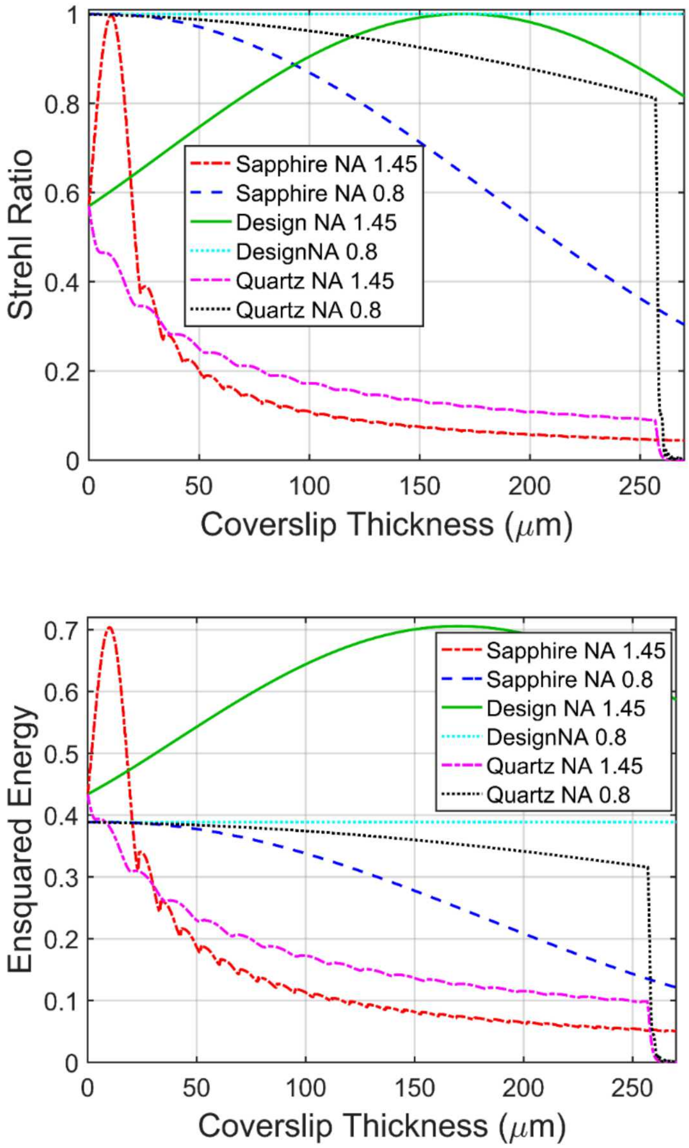

Figure 5

The Strehl ratio (a) and ensquared energy (b) calculated for a variety of potential coverslip materials at the best focus (optimum immersion oil thickness) for objectives with two different numerical aperture (NA) values. Aside from altering the NA and the coverslip index of refraction (material dependent), no other parameters were varied between simulations. Note that for an NA

1.45 objective imaging into an aqueous solution, the effective NA is limited to the index of refraction of the water, 1.3337

Software

While the effect of several non-design materials was explored in this work, open source software is provided allowing anyone to explore the effects of materials not considered here. The software was designed in Matlab R2016b (Mathworks, Natick, MA) on Windows 10, but should generally be compatible with other versions of Matlab regardless of operating system. Figure 6 shows a screenshot of the software interface and the automatically displayed results. Besides calculating the PSF, Strehl ratio, and ensquared energy for the exact refractive indices and layer thicknesses specified, the software automatically evaluates whether the Strehl ratio can be improved by using a coverslip with the specified actual index of refraction n_g but a different coverslip thickness, allowing analysis like that in Figure 1 to be trivially performed for any material. The export button outputs the results of the calculation to the workspace as two structures. The variable “Sandia_Strehl_Specific_Condition_Results” provides all the processing parameters and results for the exact conditions specified in the GUI while “Sandia_Strehl_Scan_Thickness_Results” provides the same information for the range of coverslip thicknesses considered.

The code was designed in a modular fashion, where two functions of note are specifyStrehlDefaults.m and gibsonLanni.m. Editing specifyStrehlDefaults.m allows the default parameters used by the GUI to be adjusted to match the user’s typical setup. Additionally, the default spacing to employ when evaluating possible coverslip thicknesses can be adjusted. The function gibsonLanni.m allows calculation of the Gibson-Lanni PSF, Strehl ratio, and ensquared energy independently of the GUI. In particular, it is designed to allow simultaneous calculation for vectors of different values of t_i, t_g, and t_s and could easily be extended to do the same for any of the refractive indices or thicknesses. Additionally, two Abbe number calculators are provided, allowing calculation of the approximate index of refraction at any wavelength for compounds where only n_e and V_e or n_d and V_d are known.

Simultaneously calculating the Gibson-Lanni PSF for multiple different imaging conditions offers a major improvement in computational efficiency as the Bessel function portion of the integral only needs to be calculated once as it does not depend upon the optical path.

Similarly, exploiting the radial symmetry of the PSF reduces the number of values for which the Bessel function must be determined. As such, while calculating the Bessel function is computationally expensive, calculating the Bessel function is less than 5% of the total

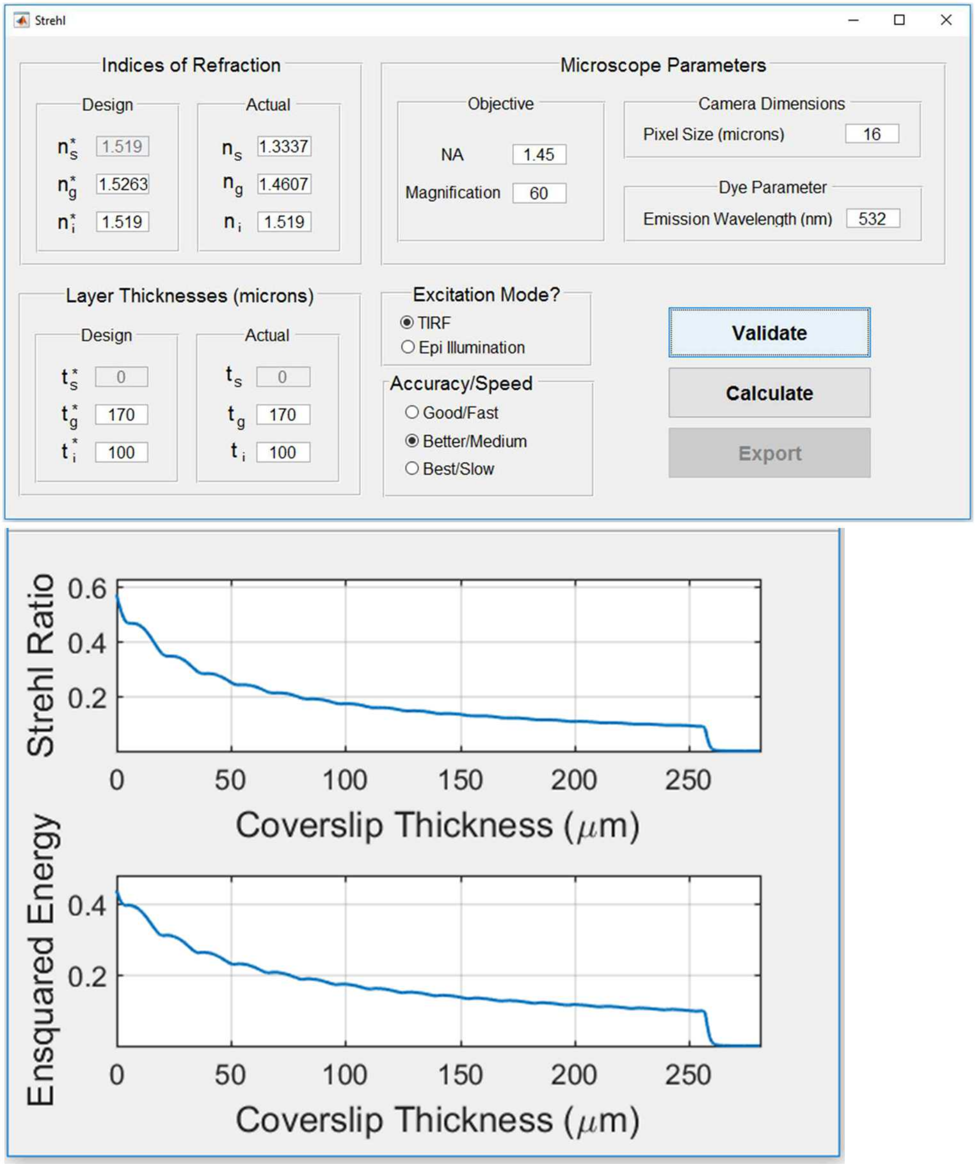

Strehl

Indices of Refraction

Design

n_s^* 1.519

n_g^* 1.5263

n_i^* 1.519

Actual

n_s 1.3337

n_g 1.4607

n_i 1.519

Microscope Parameters

Objective

NA 1.45

Magnification 60

Camera Dimensions

Pixel Size (microns) 16

Dye Parameter

Emission Wavelength (nm) 532

Layer Thicknesses (microns)

Design

t_s^* 0

t_g^* 170

t_i^* 100

Actual

t_s 0

t_g 170

t_i 100

Excitation Mode?

● TIRF

○ Epi Illumination

Accuracy/Speed

○ Good/Fast

● Better/Medium

○ Best/Slow

Figure 6

a) The graphical user interface (GUI) provided with the software developed in this work. The software is designed to make it easy for anyone to determine the effect of non-design imaging conditions on the resulting PSF. b) In addition to calculating the PSF, Strehl ratio, and ensquared energy for the exact conditions specified, the GUI also calculates the same values for the entire range of plausible coverslip thicknesses, automatically producing results like those shown in Figure 1, where the actual output of a) is shown here.

computational time when calculating the Gibson-Lanni PSF for more than 280 optical path conditions. While our code is sufficiently fast for our purposes, determining the effect of a non-design materials within under a minute, the code could likely be further optimized if desired. One obvious option would be switching to a GPU implementation in either CUDA or OpenCL, whether of just the Bessel function or a larger portion of the code. The current implementation uses standard Matlab (no mex files), and other languages might offer greater optimization. Finally, Li et al. developed “a fast and accurate approximation to the Gibson-Lanni PSF model by expressing the integral as a linear approximation of rescaled Bessel functions.”[12] Their analysis showed that their software calculated the Gibson-Lanni PSF 64 times faster than the existing state-of-the-art algorithm.[12] However, the range of non-design conditions we wished to explore extended beyond the range of conditions for which they had validated their approximation. Experimentation with their algorithm revealed that while it produced excellent results for parameters within their validated range, parameters outside that range could produce anomalous results. See Supplementary Figure 1 and discussion for more explanation. Therefore, while our analysis indicates that employing the rescaled Bessel functions would result in a roughly 3-fold speed increase, we chose not to employ that approximation at this time as we could not guarantee accuracy for all values.

One important criteria when calculating the PSF is the number of intervals to divide ρ into for integration. Dividing ρ into more intervals requires more computational time, but if ρ is divided into two few intervals, the results will be inaccurate. However, the accuracy of the calculation does not improve linearly with the computational time; if ρ is subdivided into too few intervals, the results can be wildly inaccurate. Building off of Lord Rayleigh’s quarter wavelength rule, if the optical path distance between two adjacent values of ρ does not vary by more than ¼ wavelength, the resulting calculations are unlikely to deviate substantially from the exact result. For convenience, the software developed in this work automatically checks whether any deviations exceed ¼ wavelength, warning the user if that is the case and recommending reprocessing at the next higher level of accuracy. While for most calculations in this work the good accuracy, fast setting would have been sufficient, for some materials like quartz, the better accuracy, medium speed setting was required. Therefore, for consistency all results in this work were calculated using the better accuracy setting unless otherwise specified. No results in this work required the best accuracy setting, and using a higher accuracy setting than required offers negligible benefit. As such, the best accuracy setting should rarely be required but is included to allow calculations even further from the optical design.

Conclusions

We explored how common microfabrication materials and decisions can impact the image quality for single molecule fluorescence microscopy, as measured by both the ensquared energy and the Strehl ratio. Calculations are performed using the highly popular and experimentally validated Gibson-Lanni model. The impact of non-design coverslips becomes particularly significant for high numerical aperture objectives, the type typically employed for single molecule microscopy. In fact, the effect of numerical aperture is so significant that for quartz coverslips, the image formed by an NA 0.8 objective would have a higher signal-to-noise ratio than the image formed with an otherwise equivalent NA 1.4 objective, contrary to the general conception regarding numerical aperture. These results show care must be taken when considering any modifications to the imaging system; the effects are not always intuitive, particularly when multiple modifications are combined. Additionally, we provide convenient software to facilitate easy, fast, and accurate evaluation of these effects for arbitrary materials and conditions beyond those explored in this work.

References:

1. Rust, M.J., M. Bates, and X.W. Zhuang, *Sub-diffraction-limit imaging by stochastic optical reconstruction microscopy (STORM).* Nature Methods, 2006. **3**(10): p. 793-795.
2. Whitesides, G.M., *The origins and the future of microfluidics.* Nature, 2006. **442**(7101): p. 368-373.
3. Dittrich, P.S. and A. Manz, *Single-molecule fluorescence detection in microfluidic channels - the Holy Grail in mu TAS?* Analytical and Bioanalytical Chemistry, 2005. **382**(8): p. 1771-1782.
4. Hollars, C.W., et al., *Bio-assay based on single molecule fluorescence detection in microfluidic channels.* Analytical and Bioanalytical Chemistry, 2006. **385**(8): p. 1384-1388.
5. Roulet, J.C., et al., *Fabrication of multilayer systems combining microfluidic and microoptical elements for fluorescence detection.* Journal of Microelectromechanical Systems, 2001. **10**(4): p. 482-491.
6. Smal, I., et al., *Quantitative Comparison of Spot Detection Methods in Fluorescence Microscopy.* Ieee Transactions on Medical Imaging, 2010. **29**(2): p. 282-301.
7. Haeberle, O., *Focusing of light through a stratified medium: a practical approach for computing microscope point spread functions. Part I: Conventional microscopy.* Optics Communications, 2003. **216**(1-3): p. 55-63.

8. Gu, M., *Advanced Optical Imaging Theory*. 1st ed. Springer Series in Optical Sciences, ed. W.T. Rhodes. 1999, Berlin: Springer. 214.
9. Gibson, S.F. and F. Lanni, *Experimental Test of an Analytical Model of Aberration in an Oil-Immersion Objective Lens Used in 3-Dimensional Light-Microscopy.* Journal of the Optical Society of America a-Optics Image Science and Vision, 1992. **9**(1): p. 154-166.
10. Born, M. and E. Wolf, *Principles of Optics*. 7th ed. 1999, New York: Cambridge University Press. 952.
11. Kirshner, H., et al., *3-D PSF fitting for fluorescence microscopy: implementation and localization application.* Journal of Microscopy, 2013. **249**(1): p. 13-25.
12. Li, J., F. Xue, and T. Blu, *Fast and accurate three-dimensional point spread function computation for fluorescence microscopy.* Journal of the Optical Society of America A, 2017. **34**(6): p. 1029-1034.
13. Ghosh, S. and C. Preza, *Fluorescence microscopy point spread function model accounting for aberrations due to refractive index variability within a specimen.* Journal of biomedical optics, 2015. **20**(7): p. 075003-075003.
14. Haeberle, O., et al., *Point spread function of optical microscopes imaging through stratified media.* Optics Express, 2003. **11**(22): p. 2964-2969.
15. Liang, X.J., et al., *Determining refractive index of single living cell using an integrated microchip.* Sensors and Actuators a-Physical, 2007. **133**(2): p. 349-354.
16. Shannon, R.R., *The art and science of optical design*. 1997: Cambridge University Press.
17. Standardization, I.O.f., *ISO 7944: Optics and optical instruments - Reference wavelengths*. 1998.
18. Standardization, I.O.f., *ISO 8255: Microscopes - Cover glasses*, in *Part 1: Dimensional tolerances, thickness, and optical properties*. 2017.

1. 2. NANOGAP FABRICATION

The nanogap design proposed for the LDRD's first year was to use bulk microfabrication techniques to bond a pyrex and silicon wafer together as shown in Figure 1. The silicon wafer was to have fluidic access ports, platinum electrodes, and a nanogap produced by serial ammonium hydroxide/hydrogen peroxide etching cycles. The pyrex wafer was to have a transparent ITO electrode and a deep etch well produced via HF etching to allow optimized optical access to the nanogap once the two wafers were bonded together. Unfortunately, this technique required the bonding of silicon to ITO or ITO-coated silicon to pyrex, which we were unable to produce. Anodic, plasma-assisted, and hydrogen-activated bonding techniques were all tried, but they produced only weak or partial bonds. While the nanogap creation process was highly successful, producing repeatable 15 nm gaps, we were forced to transition to a different fabrication process.

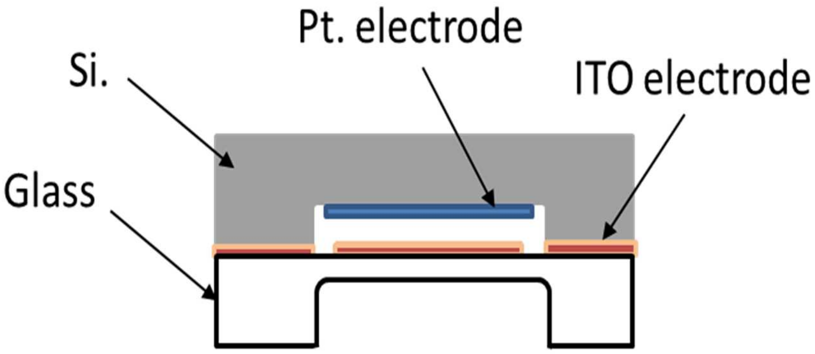

Figure 1. Initial nanogap fabrication design. Problems with the Pyrex to ITO bond prevented the realization of this structure.

Our fallback design involved the surface micromachining approach shown in Figure 2. In this design layers of sacrificial material, dielectric and metal were deposited on a pyrex wafer to build up the nanogap structure. This

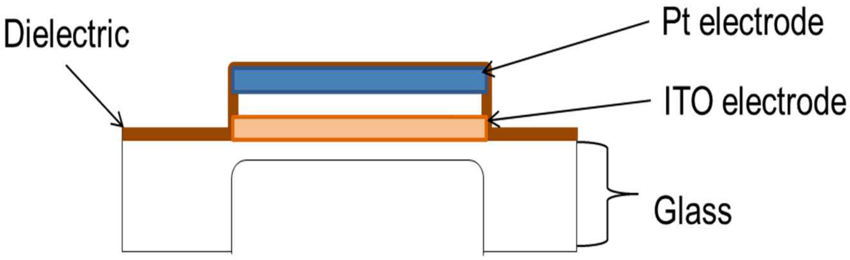

Figure 2. Our successful surface micro-machining approach to nanogap fabrication.

design produced our first electrical testing results in the program, though we were not able to use TIRF imaging in the nanogap channel as we will explain later.

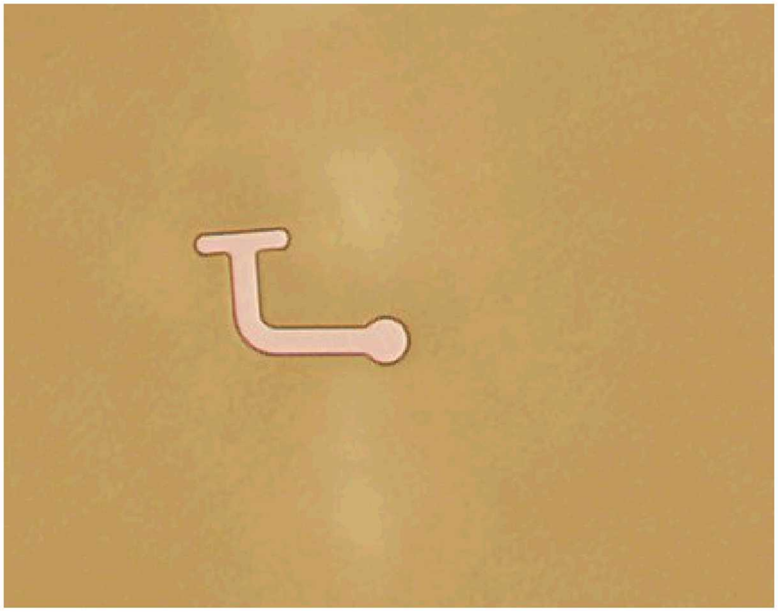

Figure 3. ITO bottom electrode defined via HCl wet etch.

Our fabrication procedure started with a high-quality commercial ITO film deposition (~ 20 ohms/square) on a 500 um thick pyrex wafer. This ITO film was both optically transparent and electrically conductive, making it the ideal bottom electrode material. We use an HCl wet etch to define the shape of the bottom electrode structure as shown in Figure 3. The electrode stack consisting of 30-50nm W, 30nm Pt, 20nm Ti was next deposited on this ITO structure. The Pt served as the top sensing electrode, the Ti helped promote adhesion between the metal stack and the following dielectric, while the W was a sacrificial material that was later etched away and would define the nanogap spacing. Two alternating layers of silicon dioxide and silicon nitride encased this stack to provide it structure and fluidic isolation from its environment. The stress of these thin films had to be carefully balanced to prevent the channel from collapsing after W removal, so a tensile nitride layer was paired with a compressive oxide layer. A series of steps then established electrical contacts to the ITO bottom electrode, the Pt. top electrode, and then encased both of these contacts in another dielectric layer to prevent shorting. Access holes were etched through the dielectric and through the top of the electrode stack to access the nanogap. Figure 4 shows a completed nanogap structure next to a scale bar for size reference. After fabrication of the surface structure, a ~320 um deep well was HF-etched into the wafer backside to allow optical access. Once singulated, individual die were cleaned and packaged for testing.

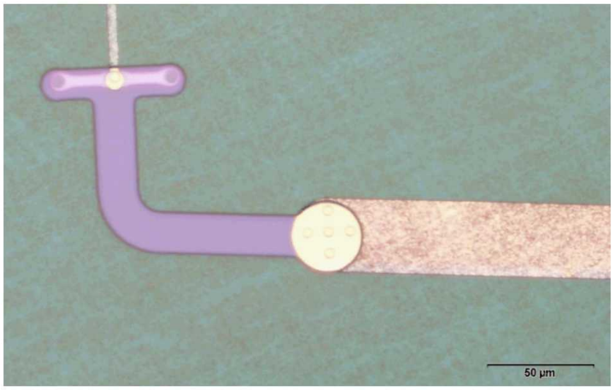

Figure 4. Completed surface micromachined nanogap electrode structure. ITO bottom electrode shown in purple connected with Ti/Au contact lines. The metal nanogap channel is shown at the top of the "T" structure.

The nanogap channels were released by etching the W sacrificial layer with hydrogen peroxide, which occurred relatively rapidly at 150 nm/min. This allowed the entire channel to be released within a few hours. Given the small etch front presented to the peroxide, we discovered that Pt or Ti remnants or stringers could greatly impair channel release. To compensate for this we later transitioned to exposing the channel to a dilute aqua regia etch prior to W release. Given the small, 30-50 nm, gap in the channels there was concern that capillary forces from drying liquids would collapse the channels once they were released. To prevent this, once the channels were released the die was stored in a fluid.

These initial devices provided the first verification of the design's electrical functioning, but they were unable to provide sufficient optical access to the nanogap for TIRF imaging. It was eventually determined that pyrex's index of refraction was insufficient to allow optimized imaging, even at the 180 um imaging window thickness.

To compensate for this material shortcoming, the above fabrication process was repeated on soda lime wafers. While the soda lime substrate was generally an adequate substitute for pyrex during fabrication, it was not amenable to production of the optical access window via deep HF etching. Soda lime etches more slowly in HF compared to pyrex, and it produces cloudy metal oxide deposits during etching. These oxides can be eliminating with a HF/HCl wet etch, but this resulted in a long and labor-intensive process. Instead of an etch window, the individual die were polished to a thickness of 180 um using wafer lapping/polishing equipment in the fab. With this final process change, we were able to produce devices that allowed TIRF access and single molecule optical detection in the nanogap channels.

3.Description of the Custom-Built Potentiostat

PART 1: THE FUNCTION OF OUR CUSTOM-BUILT POTENTIOSTAT.

THE CUSTOM BUILT POTENTIOSTAT REQUIREMENTS WERE AS FOLLOWS:

1. Measure current, as low as 10fA, that originates from each of two independent **Working Electrodes** (which are the electrodes inside the micro-channel.)
2. Maintain a set potential for each of these two independent **Working Electrodes**, in respect to a **Reference Electrode**.
3. A commercial Ag/AgCl **Reference Electrode** is situated outside the micro-channel, and has a continuous path for ionic conductivity into the micro-channel. Its potential is measured accurately only if no current is allowed to flow through it.
4. A **Counter Electrode**, which is also situated outside the micro-channel, serves to collect the return current from <u>both</u> working electrodes. Since the reference and counter electrodes are closer together and are emerged in a solution reservoir, the counter electrode potential is set automatically, by a negative feedback circuit, such that **Reference Electrode** potential remains at the "ground" or "chassis" potential.

The ground potential would act as the reference to all the potentials in the system and the working electrodes' currents will be measured when flowing to this ground.

PART 2: SETTING THE WORKING ELECTRODES' POTENTIALS

The Potentiostat is controlled by a LabView code, which communicates with the hardware by means of two National Instruments USB OEM boards: ***A.*** NI-USB-6366-OEM board with 16x digital outputs, 2x 16-bit digital-to-analog (D/A) outputs and 8x relatively fast (2.0 MS/s) 16-bit analog-to-digital (A/D) converters, and ***B.*** An inexpensive NI-USB-6001-OEM for supplementa 2x 14-bit digital-to-analog (D/A) output channels with more auxiliary 20kS/s 14-bit A/D and digital input/outputs.

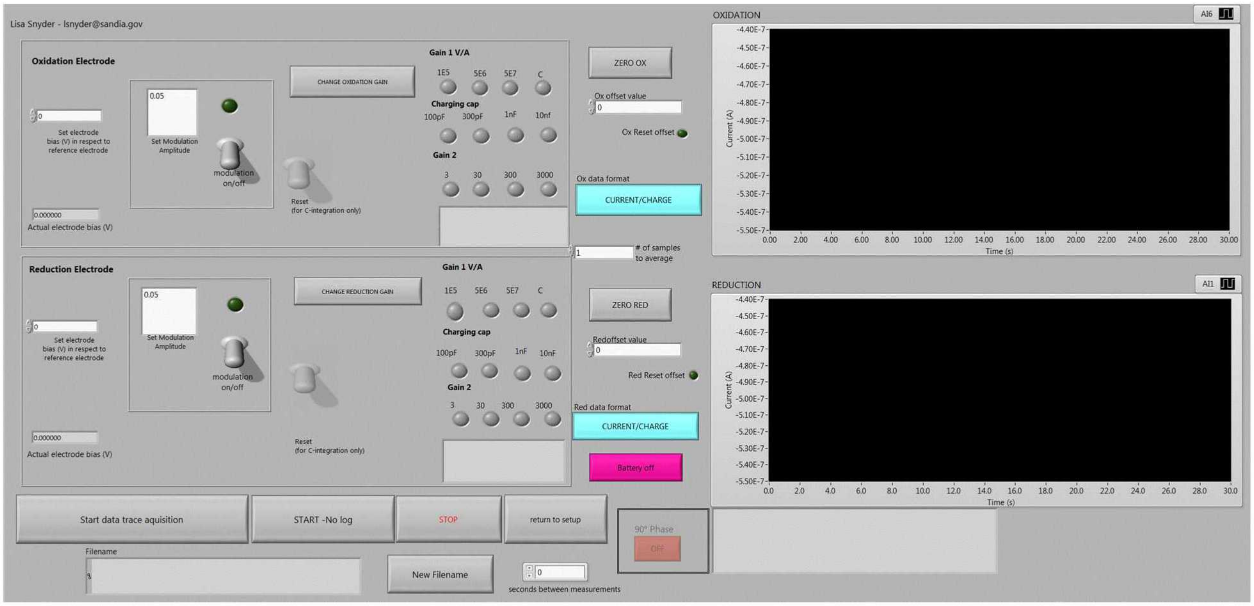

Set electrode bias (V) in respect to reference electrode: 0
Set Modulation Amplitude: 0.05
Actual electrode bias (V): 0.000000
Ox offset value: 0
# of samples to average: 1
Set electrode bias (V) in respect to reference electrode: 0
Set Modulation Amplitude: 0.05
Actual electrode bias (V): 0.000000
Redoffset value: 0
Filename: %
seconds between measurements: 0

Figure 1. A virtual LabView panel for the Potentiostat, showing separate bias, modulation, current-sensing options and current vs. time displays for the two independent working electrodes (Reduction and Oxidation.)

The main LabView virtual panel of the Potentiostat is shown in Fig. 1. Two horizontal rectangular sub-panels named "Oxidation" and "Reduction "are used to set and monitor the two independent working electrodes. The left side of these panels is where the operator sets the electrodes' bias in respect to ground (which is also the box chassis and the Reference Electrode potential), with the option of adding a 1kHz sinewave modulation at a user-defined amplitude. The optional addition of a bias modulation, if it results in modulation of the redox current, and its detection with a Lock-In detector scheme, can theoretically enhance the signal-to-noise ratio dramatically.

Figure 2 shows the schematics of the portion of the Potentiostat that produces the bias for each working electrode (it is identical for both):

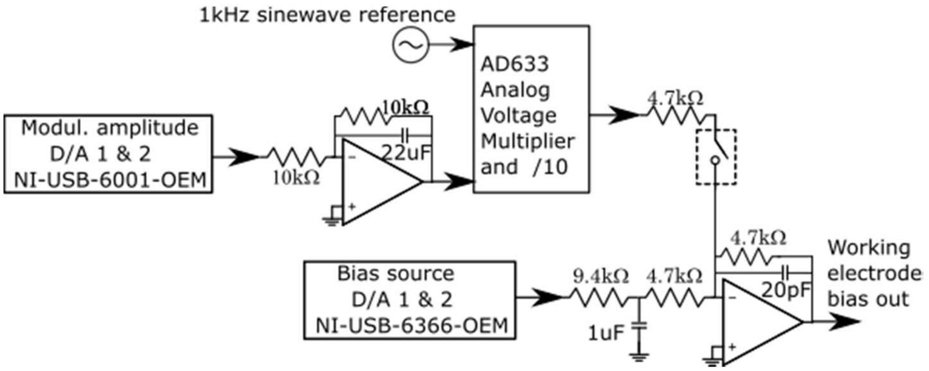

Figure 2 Schematics of the working bias generation

The requested working electrode bias is set x3 higher on the D/A channels for each electrode, and is filtered and divided by 3 to obtain a higher resolution and a lower noise level. The D/A channel has an output range of +/-10V, while the actual bias should never exceed +/- 3.3V. If the user desires to superimpose a low voltage modulation on top of the bias, for a later Lock-In amplifier detection scheme, the modulation amplitude X100 is generated from a lower quality D/A source. This D/A output is well –filtered for high frequency noise, and then it is multiplied by a 100mV amplitude 1kHz sinewave reference signal, and divided by 10.

Note that triangles represents an operational amplifier (Op-Amp). Unless otherwise noted, these Op-Amps are AD822 (dual) and LT1122 (single) , FET-based, with low input bias currents . All the switches that are surrounded with a dashed box are controlled by the 3-5V digital signal from digital outputs on the NI boards. These switches are ADG1404 (quad, SPST), DG468 (single, SPST), or DG449 (single, SPDT, break-before-make.)

The circuit is powered with +9V and -9V from two 9V battery packs to avoid external noise. All the above components can operate well with a bipolar +9V/-9V supplies. To avoid cross talk between components, the +9V/-9V supply voltages were fed through a 10Ω resistor, followed by a 22uF capacitor to ground before connecting to each integrated circuit. Also, the printed circuit board (PCB) had 3 metal layers for routing the signals between the soldered components. To further remove noise and cross talk, metal layers 2 and 4 were designed as continuous sheets and tied to the analog chassis ground. Additionally, signal lines were spatially separated from interfering lines, especially from lines carrying the 1kHz modulation.

PART 3: PROVIDING BIAS TO, AND SENSING CURRENT FROM WORKING ELECTRODES

Since we want to measure very find current values on the come from the electrodes, we wish to avoid leakage between the center lead in a coax cable and the grounded shield. To ensure that this is the case, we use a **Triax** cable with two concentric shields, and keep the inner shield in the same potential as the center lead that contacts the working electrode.

Figure 3 presents the schematics used for sensing the current from a working electrode while maintaining it at the desired bias.

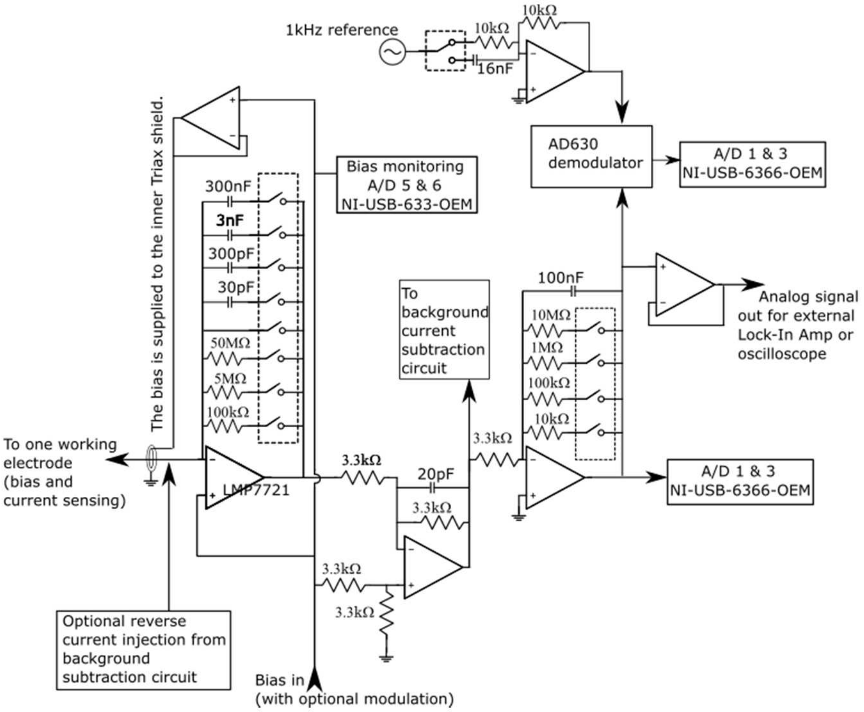

Figure 3 The schematics of the main circuit for each working electrode, which biases, senses and amplifies the current, and if a modulation was added to the bias, extracts the signal after demodulation.

The bias is fed from the circuit in Fig. 2 to the bottom of this circuit drawing. It is copied to the Triax center shield through a repeater, such that if it shorts to any other ground or signal, it would not affect the main circuit. The main transimpedance amplifier (current-to-voltage converter, using a Texas Instruments LMP7721 Op-Amp) rides on the bias, and hence, as long as the current coming from the working electrode is not too high to saturate the Op-Amp's feedback loop, it will maintain the electrode at the desired voltage very accurately (< 1mV). LMP7721 was selected because it is the industry's lowest specified input bias current precision amplifier, with an ultra-low input bias current is 3 fA (specified limit of ±20 fA at 25°C). It also has a very low voltage noise (6.5 nV/√Hz) and low DC-offset voltage. However, since the LMP7721 works at lower voltages, two LM185H-2.5 Zener diodes with 22uF capacitors were used to drop the ±9V supplies to very stable ±2.5V. The down side is that the bias is now limited to roughly ±1.5V if one wants to maintain a reasonable working current measurement range.

Two of the three rows of round buttons in the virtual instrument panel (Fig. 1), for each working electrode, control the 8 switches that kick in each feedback option for the LMP7721 Op-Amp. Connecting each of the 3 resistors (one at a time) gives rise to transimpedance gain of 10^5, $5x10^6$, and $5x10^7$ Volts/Ampere. While a particular resistor is connected, each of the capacitors can be switched as well, acting as a stronger low-pass filter with increasing capacitance value. Alternatively, if a capacitor is switched while no resistor is connected (using the button with the "C" notation), the circuit integrates the current and produces a signal that is proportional to the cumulative charge. Closing the short switch can zero the integrator if it saturated. Finally, to ensure that the short line does not leak when disconnected, we used 4 independent switches in series (not shown here).

After the transimpdance conversion to voltage, the bias is subtracted from the LMP7721 output and the voltage that is now proportional to the electrode current with no offset goes into a stage 2 amplifier, with selectable gains of 3.3, 33, 330, and 3300. The final signal is fed into an A/D converter and displayed continuously vs. time on a moving chart in the right hand side of the virtual instrument panel, as well as saved as a CSV file (current and bias voltage vs. time for each working electrode), if desired . The program computes the current value out of the final voltage depending on the gain resistors selected. To further remove noise, the LabView code offers averaging of ant number of measurements into a single point on the graph or in the CSV file. Since the data acquisition is much faster than the drawing, oen can average almost 1000 points for each measurement without noticing a slowdown.

When a modulation is added to the bias, the voltage signal that represent the working electrode current would be also modulated. If we choose a working electrode potential that is close to the detection limit of the redox reaction of interest, the resulting current modulation is expected to be large. The AD630 integrated circuit will use the reference sinewave signal to pick up that modulation amplitude. Note that the reference sinewave can be delivered to the AD630 with a 90° phase shift in comparison to the bias modulation, to compensate for system response delays. For a better de-modulation, the user can use the buffered output signal with an external commercial Lock-In Amplifier.

PART 4: SUBTRACTING BACKGROUND CURRENT TO ALLOW HIGHER GAIN.

Dealing with wet chemistry when attempting to measure femto-Amps is a problem. Depending on the electrode biases, the KCl solution that we use to move charge to the counter and reference electrodes may conduct. Even the dry DATL device had only 1MΩ between the two working electrodes due to some conducting residues. To enable gain increase that is sufficient for detecting such small signals, the background/leakage currents need to be cancelled at the source, by injecting current of the opposite sign to the electrode.

Figure 5 shows the simple circuit that can do it with a feedback loop, similarly to an oscilloscope working at AC vs. DC mode, where the baseline is subtracted in real time. The only difference here is the time scale: The feedback loop has to be substantially slower to be able to pick up the slow anticipated current peaks (ms to s) after the gain was increased, one step at a time.

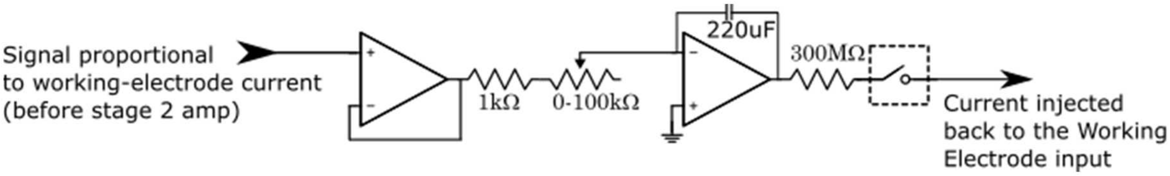

Figure 4 Subtracting background current by injecting the opposite current from a slow (adjustable gain) feedback loop.

A manual variable resistor (100 kΩ potentiometer) is installed on the electronics box, one for each working electrode, to allow the user to start with a faster feedback loop and slow it gradually when starting the actual measurement.

PART 5: COUNTER AND REFERENCE ELECTRODE.

As described above, we chose to keep the Reference Electrode at ground potential, so we can have all the potentials in the system referenced to ground, which gives us a higher range of biases and measurable currents. Figure part shows the simple integral feedback loop used to control the counter electrode voltage:

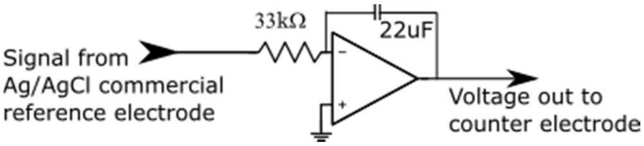

Figure 5 A simple integral-based negative feedback loop that would supply a voltage to the counter electrode that will cause the reference electrode output to stay at ground potential.

The feedback is sufficiently slow enough to filter potential 60Hz noise.

PART 6: TESTING AND CALIBRATION.

A cyclic voltamogram recording option was added to the LabVIew software, that allows one or both working electrodes' bias voltages to be swept linearly back and forth continuously, between two voltage values (separate foe each electrode). The recorded current can aid in selecting the correct working potentials.

Testing the action of the Potentiostat is easily done by setting a DC bias on one working electrode Triax connector, and placing a resistor with a known resistance value between the inner lead (electrode) and the outer shield (ground). Selecting different values for the gains of the 1st (transimpedance) and the 2nd (voltage-to-voltage) amplifier stages, one can determine the true gains and type them into a parameter page in the LabView program for more accurate current display. At this point, zeroing the background can be tested, as well as adding modulation and looking at the resulting current output (i.e., the analogvoltage signal output in fig. 3) on an oscilloscope.

The counter electrode can be tested by placing a resistor between the counter electrode output to the reference electrode input. The voltage on both sides of the resistor should zero within 1s.

When the potentiometer is connected to the DATL device, with the Reference and the Counter electrodes dipped into a drop of solution that covers the device, it is important to test as follows:

1. Have the counter electrode disconnected and make sure that upon any abrupt change of one electrode potential, or applying a potential-sweep (cyclic-voltamogram mode), the two working electrodes measure the same current vs. time patterns, except at opposite polarity.
2. To ensure an open path for ions flow between the solution drop (reservoir) and the channel, replace one working electrode with the counter electrode. Once again, ensure that upon any abrupt change of the connected channel working electrode potential, or applying a potential-sweep, the counter electrodes shows the same current vs. time patterns as the channel working electrode, except at opposite polarity, as is demonstrated in fig. 6.

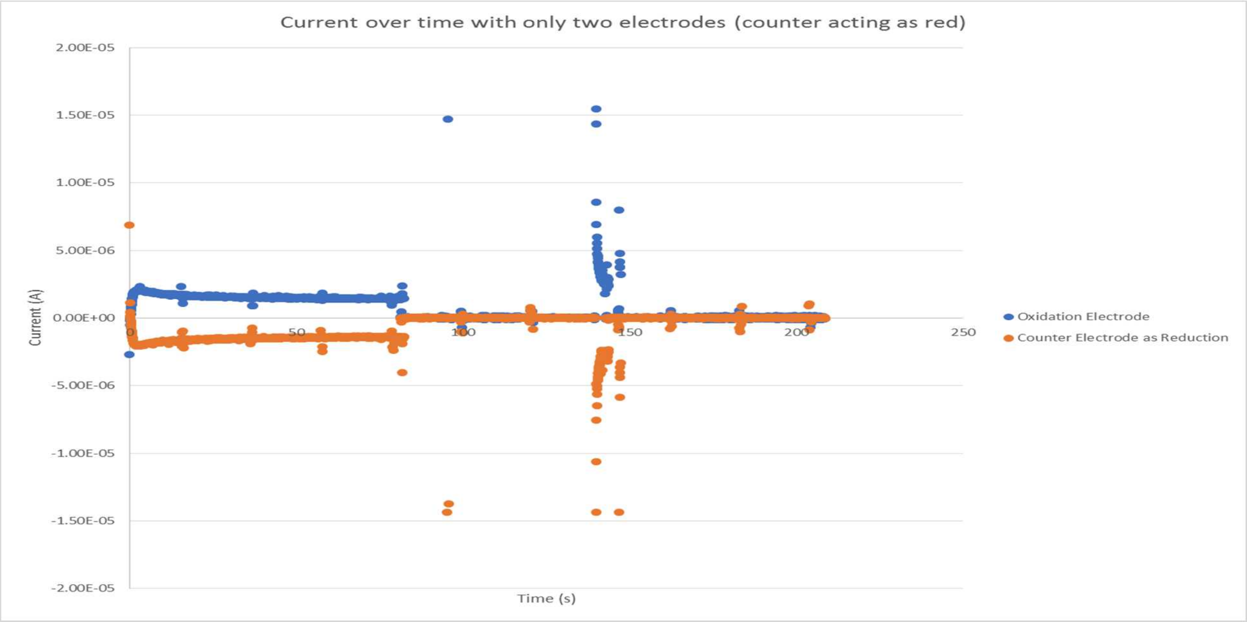

Figure 6 Using an 0.1M KCl solution in a large drop that covered the DATL device, one working electrode in the channel was connected to one Potentiostat channel while the second channel was connected to the counter electrode outside the channel. The blue and the orange plots show the current recorded in both channels upon arbitrary changes in the channel working electrode potential. The identical temporal patterns but with opposite polarity of the measured signals indicate that there is a clear path for ions to flow between the micro-channel and the drop reservoir.

PART 7: CONCERNS REGARDING THE CORRECT FUNCTIONING OF THE ELECTROCHEMICAL SYSTEM.

The original work from the Lemay group assumed that when a single analyte molecule enters the micro-channel, it is able to travel back and forth between the two working electrode,oxidizing on one and reducing on the other. Hence, when the authors detected similar current pulses as a function of time on both electrodes simultaneously (only reversed in polarity), they took it as evidence that both oxidation and reduction were indeed happening as long is that molecule was moving in the gap. However, one must keep in mind that when the two working electrodes are so close, and the counter electrode is separated by an ion-transport limited path, it is very likely that one working electrode was simply returning the current that the other working electrode only has sunken or sourced.

A future such DATL device may be somewhat improved if designed with a shorter micro-channel, and a horn/funnel-shaped connection to a solution reservoir on each side. The counter and reference electrodes should be placed in one of these reservoirs and reside in closer proximity to the working electrodes.

4. Computational approach for modeling single molecule detection

Computational studies were designed to support experimental efforts and clarify mechanisms leading to current build up due to redox cycling, diffusion and adsorption of single molecules undergoing redox reactions. Three different types of simulation methods were implemented for this project. The interaction between ITO surface and redox molecule, $Ru(bpy)_3^{2+}$ is simulated using highly accurate quantum simulations. The hydration of $Ru(bpy)_3^{2+}$ was studied using all atom molecular dynamics simulations. The molecular dynamics simulations were also used to calculate diffusion constants which was later used in random walk simulations to calculate power spectral density for a particular sensor geometry.

FIG. 1: $Ru(bpy)_3^{2+}$ molecule interacting with an ITO surface. ITO surface is composed of total 264 atoms $(In_{84}Sn_{12}O_{144})H_{24}$ with hydroxyl groups at the surface.[1] VASP molecular dynamics simulation package was used for calculations.

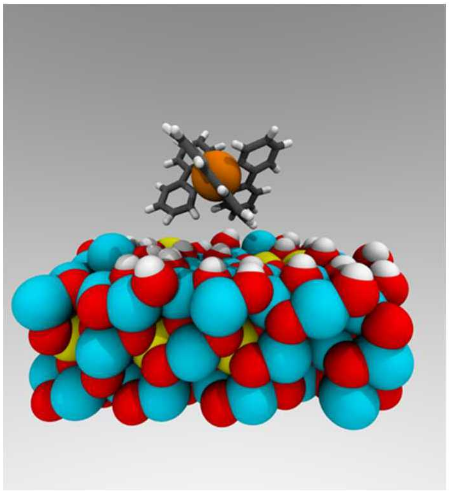

Ab initio molecular dynamics

The quantum based *ab initio* simulations permit investigation of fundamental electron transfer between redox molecules and sensor materials. The high-resolution simulations track electron movement and can be useful in understanding quantum level interactions between the sensor and molecule of interest. The simulated system is shown in FIG. 1. After initial equilibration of ITO surface,[1] charge transfer between $Ru(bpy)_3^{2+}$ was calculated. The initial simulations in periodic boundary conditions showed the $Ru(bpy)_3^{2+}$ transfers 20% charge to the surface hydroxyl groups. The goal of calculating redox potential was not achieved due to complex and sluggish nature of the system.

Classical molecular dynamics simulations

Classical molecular dynamics simulations allow large time-scale and are useful for calculating transport properties in solution. We used these simulations to calculate diffusion constant of $Ru(bpy)_3^{2+}$ in water. The classical MD simulations use Newton's equation of motion to produce simulation trajectories. The system consists of single $Ru(bpy)_3^{2+}$ in 1000 water molecules is shown in FIG. 2(a). After initial equilibration of the system, 10 ns of production run was simulated for analysis. The radial distribution function between Ru and water oxygen (Ru-Ow) (FIG. 2 (b)) shows a first peak at around 0.8 nm. The pyridine rings around ruthenium atom pushed water away from the center. The small plateau on radial distribution function at 0.5 nm corresponds to water trapped inside gaps of pyridine rings.

Diffusion constants of $Ru(bpy)_3^{2+}$ was calculated from the slope of mean square displacement (MSD) plot. The diffusion constant of $Ru(bpy)_3^{2+}$ was 8-10 X 10^{-11} m^2/s at 300 K. The salt concentration did not have any effect on the diffusion constant. This value was used for random walk simulations.

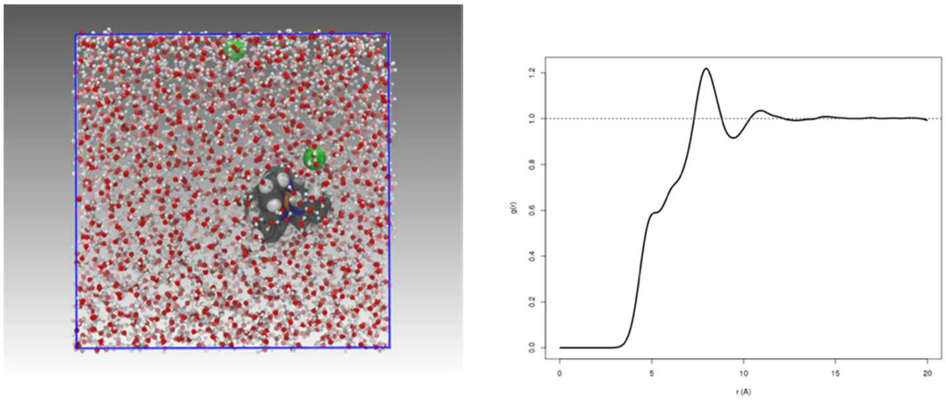

FIG.2: (a) System containing single $Ru(bpy)_3^{2+}$ in 1000 SPC/E water molecules in periodic boundary conditions. Gromacs molecular simulations software was used for simulations. (b) Radial distribution function between Ru and water oxygen (Ru-Ow).

Random walk simulations

Diffusion based modeling[2,3,4] can be used to test different sensor geometries. The input parameter for the simulations are diffusion constants, adsorption/desorption probabilities and sensor dimensions. These simulations are designed to mimic the experimental power spectral density to calculate the adsorption/desorption rate for a particular geometry and electrode. The objective of these simulations was to fine-tune sensors.

A C++ based random walk simulation code developed by Kätelhön and co-workers[3,4] was used for the project. The aim was to modify the code for our sensor geometry and our molecules of interest to simulate and fine-tune sensor performance. A simple rectangular sensor geometry was shown in FIG. 3(a). A power spectral density obtained in one of the cases where redox molecule is adsorbed onto the sensor surface is shown in FIG. 3(b).

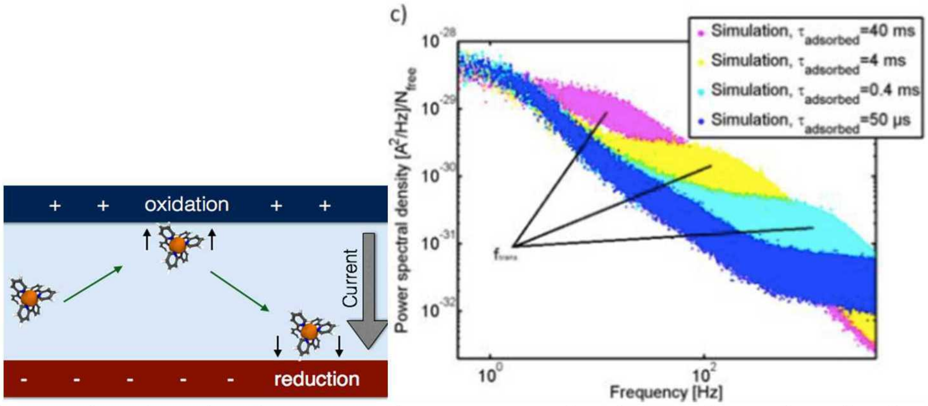

FIG. 3 (a) Picture showing simple rectangular sensor and redox cycling of Ru(bpy)32+ molecule. (b) Power spectral density published in ref. 4 at several different adsorption times.[4]

1. “Study of the Redox Properties of Singlet and Triplet Tris(2,2′-bipyridine)ruthenium(II) ([Ru(bpy)3]2+) in Aqueous Solution by Full Quantum and Mixed Quantum/Classical Molecular Dynamics Simulations.” Polydefkis Diamantis, Jérôme Florian Gonthier, Ivano Tavernelli, and Ursula Rothlisberger, **J. Phys. Chem. B,** 2014, vol. 118 (14) pp. 3950-3959. http://dx.doi.org/10.1021/jp412395x
2. “Brownian motion in electrochemical nanodevices”, K. J. Krause, K. Mathwig, B. Wolfrum, and S. G. Lemay. **Eur. Phys. J. Spec. Top.**, 2014 vol. 223 (14) pp. 3165-3178. http://link.springer.com/10.1140/epjst/e2014-02325-5
3. “Noise Phenomena Caused by Reversible Adsorption in Nanoscale Electrochemical Devices.” E. Kätelhön, K. J. Krause, K. Mathwig, and S. G. Lemay, **ACS nano,** 2014, vol 8 (5), pp 4924-4930. http://pubs.acs.org/doi/abs/10.1021/nn500941g
4. “Noise Characteristics of Nanoscaled Redox-Cycling Sensors: Investigations Based on Random Walks.” Enno Kätelhön, Kay J. Krause, Pradyumna S. Singh, Serge G. Lemay, and Bernhard Wolfrum, **J. Am. Chem. Soc.**, 2013 vol. 135 (24) pp. 8874-8881. http://pubs.acs.org/doi/abs/10.1021/ja3121313

2. DISTRIBUTION LIST

1	MS 0899	Technical Library, 9536 (electronic copy)
1	MS 0359	Donna Chavez, LDRD office, 1911

Sandia National Laboratories